DOI: 10.13009/EUCASS2017-40

Analytical and numerical assessment of axial thrust balancing systems in liquid rocket engine LOx turbopumps

S. Maier*, B. Wagner*†, L. Veggi**, J. D. Pauw**, P. Beck**
*DLR - German Aerospace Center
Institute of Space Propulsion, Turbomachinery in Rockets
Lampoldshausen, 74239 Hardthausen, Germany
**Technische Universität München - TU Munich
Chair of Turbomachinery and Flight Propulsion, Section Space Propulsion
Boltzmannstrasse 15, 85748 Garching, Germany
...
†Corresponding author: Bernd.Wagner@dlr.de

Abstract

Different pressure profiles on the frontside and backside of radial impellers create forces in axial direction. In high head turbopump assemblies for liquid rocket engines axial thrust is inevitable, especially during start-up transients, harsh environment operations, and throttling. Various passive and active axial thrust balancing systems exist. This paper concentrates on active systems, where the rotor assembly moves axially to compensate unbalanced axial force and the hub of the impeller acts as a balance piston. The function of two systems will be described. Analytical and numerical methods are applied to determine axial forces. The analytical formulations of each part in the system of an active balancing setup are implemented into a program and it is verified and validated with results from simulations. The numerical method also is validated and shows good agreement with data from literature. In a case study of a 120 *kN* engine LOx turbopump impeller, analytical and numerical results for the axial forces and the leakage flow are presented for an active balancing system with one governing gap and for a system with two governing gaps. Calculations have been done for three rotation speeds and a rotor displacement of 0.5 *mm* around the nominal position. The results are shown and discussed.

1. Introduction

Expertise in designing turbopumps is being built up in Germany. In the course of this the project KonRAT, a German abbreviation for application of rocket propulsion components for aerospace transport systems, has been founded at the Ludwig Bölkow Campus in Bavaria. Key objectives of this project are establishing design procedures within turbopumps for cryogenic oxygen, investigations of selected problems in turbopumps and additive manufacturing methods for aerospace applications like turbopump parts and rocket engine valves. One of the work packages covers the aspect of secondary systems. Besides the main flow path through the inducer and the impeller on the side of the pump and the stator and the rotor on the side of the turbine, several additional fluid systems and fluid paths exist in turbopumps for liquid rocket engines, for example the flow through bearings for lubrication and cooling needs and through the seals as leakage and purge flow but all kind of gap flows, too. Different pressure levels on fluid exposed areas in those gaps cause forces in axial direction. Thus, in turbopump assemblies axial thrust is inevitable. In this context the secondary flow systems in the rotor stator cavities of the impeller play a major role. In order to reduce the forces on the already highly loaded bearings the axial thrust should be predicted precisely and minimized by design.

Rotor bearings in turbopumps for liquid propellant rocket engines (LRE) are highly loaded components. Typically they are operated at very high rotational speeds and under cryogenic conditions while being lubricated by the medium conveyed (e.g. oxygen, methane or hydrogen in liquid form), which generally has very low viscosity and therefore low lubricational quality. Under these circumstances the bearings are supposed to have as little rolling resistance as possible. If the propulsion system is meant to be reusable, the demands for service life towards the bearings will be even higher. As a consequence, the load on these must be kept as low as possible. Because of the high pressure level and different pressure distributions in the side cavities of the impeller there would be a large amount of axial thrust if no measures were taken to balance axial forces. This would mean a high load on the rotor bearings and would

Copyright © 2017 by S. MAIER; B. WAGNER; L. VEGGI; J.D. PAUW; P. BECK Published by the EUCASS association with permission.

DOI: 10.13009/EUCASS2017-40

significantly reduce their service life. Therefore axial thrust balancing plays an important role in increasing reliability and in extending service life of bearings in turbopumps for LRE.

2. Background on Axial Balancing

Axial thrust on the rotor assembly emerges from different types of forces, for example pressure forces, impulsive fluid forces or gravitational forces. Typically, pressure forces acting on the impeller account for the most part of axial thrust. Thus, efforts towards balancing concentrate on this part of the turbopump. Because of centrifugal forces, the pressure in the cavities between casing and impeller on both its sides generally decreases from the high impeller exit pressure at the impeller outer radius to lower pressure levels towards the center. Furthermore, the pressure distribution on the suction side of the impeller drops down sharply to suction pressure level at a labyrinth seal or slip ring seal located at the inner end of the suction side cavity. On the backside of the impeller there is no such sharp drop of pressure. Since areas on both sides of the impeller, which the pressure acts on are usually about the same size, an imbalance in axial thrust arises as a result of the different pressure profiles.

2.1 Passive Axial Balancing Systems

Measures to balance axial forces usually aim to change the pressure distribution on the backside of the impeller so that there is an equilibrium under steady state conditions. The imbalance during transient operation is kept to a level which the rotor bearings can handle. The behavior of passive systems is not affected by a displacement of the rotor and axial forces are in balance just for a specific point of design. Passive balancing can be achieved by installing a labyrinth seal or a annular gap seal and back flow holes on the backside of the impeller to match the pressure distribution on both sides. Other options are impeller back vanes and balancing holes which increase the leakage flow in the backside cavity. Both measures increase the fluid rotation and thus decrease the axial force.

2.2 Active Axial Balancing Systems

In active systems the pressure distribution in the backside cavity and therefore the axial force towards the suction side sets in according to the displacement of the rotor assembly. Annular and radial gap orifices are used to create this effect. A change in nominal axial force results in rotor movement which leads to the change of the width of one or more gaps in the balancing system. As a consequence, the axial balancing force will change. Once axial forces are balanced, the rotor assembly will stop moving. Therefore active systems can adjust to altered operating conditions.

2.2.1 Balancing System with One Governing Gap

Active balancing systems with one governing gap typically incorporate an annular gap in the outer region of the impeller backside and an axial gap between casing and impeller backside at an inner radius. Further inside from the axial gap there are holes for the leakage flow to return into the main flow channel to a location with low pressure. In some cases the gap flow goes through bearings for cooling purposes before reentering the impeller main flow. Active systems generally involve a leakage flow from the impeller outlet through various gaps and balancing holes back into the main flow. Thus pressure losses occur across narrow gaps which depend on the amount of leakage and the gap width. In a system with one governing gap there is a first pressure drop at the annular gap. As a consequence the pressure level in the backside cavity of the impeller generally decreases and so the axial force towards the suctions side is reduced. As a result of centrifugal forces pressure decreases further towards the center. A second pressure drop down to almost suction pressure level occurs at the axial gap. Across the balancing holes and the cavity in front of these there is only a slight pressure loss. Consequently, the width of the axial gap or the displacement of the rotor assembly respectively determines the level of pressure in the backside cavity of the impeller and thus the level of axial force towards the suction side.

2.2.2 Balancing System with Two Governing Gaps

The basic layout of a balancing system with two governing gaps is similar to the system with one governing gap. The axial gap, the balancing holes and the impeller backside cavity are configured in the same way. The annular gap is replaced by a second axial gap at the outer radius of the impeller. It is designed in a way so that it closes when the inner axial gap opens. In these systems there is also a leakage flow that runs through the backside cavity, including both axial gaps and so, depending on their width, causing pressure losses across them. The pressure level and thus the axial force

DOI: 10.13009/EUCASS2017-40

towards the suction side is determined by both axial gaps in such a system. In case the rotor assembly moves towards the suction side, the outer gap closes and the inner gap opens, which results in a bigger pressure drop across the outer gap and a lower pressure drop across the inner gap. As a consequence, the pressure level in the backside cavity and the axial balancing force decrease. If the rotor assembly moves in the opposite direction, the pressure level and the balancing force increase.

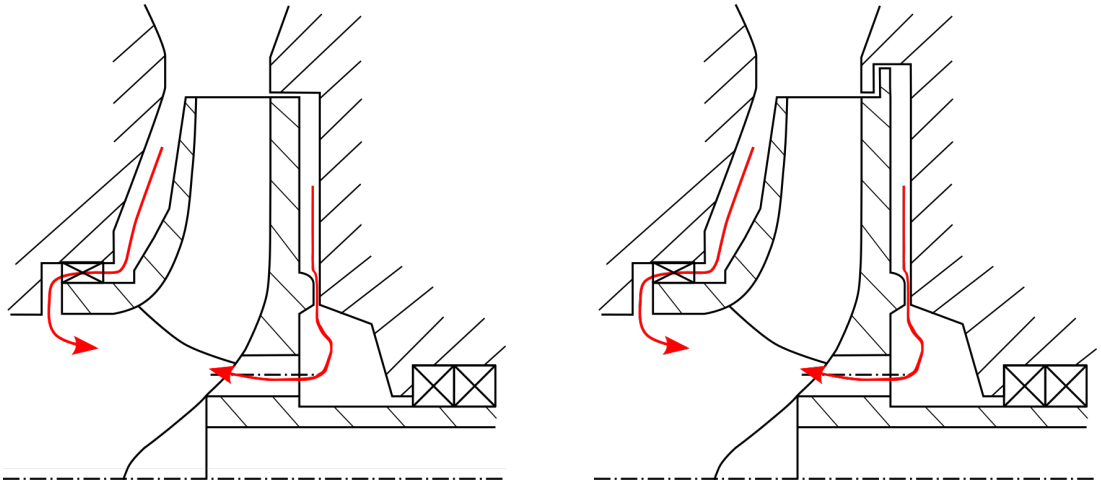

Figure 1: An axial balancing system with one governing gap system (left) and a system with two governing gaps (right)

2.3 Description of the Flow

2.3.1 The Flow inside a Rotor-Stator Cavity with superposed Throughflow

In calculations for pressure and axial force acting on the impeller the flow inside a rotor-stator cavity with superposed throughflow plays a key role. In such a cavity the fluid is at no-slip at the stator wall and at the rotor wall. Therefore the fluid is at rest at the casing wall and rotates with the local tangential velocity at the impeller wall: $c_u = \omega\, r$. There are boundary layers on both sides of the cavity. In those, the tangential velocity c_u decreases from the rotating wall towards the center of the cavity and it increases from the casing wall towards the center. There are various types of flow that can form in a rotor-stator cavity. Daily and Nece [3] have identified four flow regimes in their work:

Flow Regime I: laminar flow and boundary layers interact
Flow Regime II: laminar flow and boundary layers are separated
Flow Regime III: turbulent flow and boundary layers interact
Flow Regime IV: turbulent flow and boundary layers are separated

If the boundary layers are separated a core region forms where tangential velocity is constant. In turbopumps for LRE typically a flow of regime IV is present. The discussion in the present paper therefore focuses on that type of flow. The rotation of the fluid causes centrifugal forces. Since rotation is higher next to the impeller wall than next to the casing wall, fluid is conveyed outwards. For continuity reasons, the fluid flows back inwards at the casing wall. Thus, a circulation of fluid forms in the meridional plane and boundary layers form at the rotor and the stator wall. To describe the flow in a rotor-stator cavity the fluid rotation ratio

$$k = \frac{\beta}{\omega} = \frac{c_u\, r}{\omega} = \frac{c_u}{u} \tag{1}$$

is introduced. It describes the relation between local rotational fluid speed in the core region β and the impeller rotational speed ω. If there is no throughflow, k is constant: $k(r) = k_0$. In the core region the gradient in pressure equals the centrifugal force:

$$\frac{dp}{dr} = k^2(r)\,\omega^2\, r^2\, \rho. \tag{2}$$

If the pressure p_2 at the outer radius r_2 of the cavity is given, the pressure distribution can be calculated with

$$p(r) = p_2 - \rho\,\omega^2 \int_r^{r^2} k^2(r)\, r\, dr. \tag{3}$$

DOI: 10.13009/EUCASS2017-40

The axial force acting on the rotor can be quantified using

$$F_R = \int_{r_N}^{r^2} p(r)\, r\, dr. \tag{4}$$

Zilling [13] found a correlation for the fluid rotation ratio k_0 in rotor-stator cavities without throughflow based on their geometry:

$$k_0 = \frac{1}{1 + \left(\frac{r_W}{r_2}\right)^2 \sqrt{\left(\frac{r_W}{r_2} + 5\frac{t_{ax}}{r_2}\right) C_{f,W/R}}} \tag{5}$$

with $C_{f,W/R} = \frac{\lambda_W}{\lambda_R} = \frac{\lambda_U}{\lambda_R}$ being the relation between the friction coefficient of the stator wall and the rotor wall. The equation accounts for fluid wall friction at the rotor, the stator wall, at the outer casing wall and at the hub wall. The boundary layers at those walls are considered to be similar to a turbulent pipe flow and the radius of the hub to be negligible.

In turbopumps for LRE a leakage flow that runs from the impeller outlet with a high pressure level to the impeller inlet with a low pressure level passing through the impeller side cavity exists. It flows along the casing inwards and carries along the angular momentum of the main flow. Thus, the leakage flow boosts the fluid rotation in the impeller side cavity. With a superposed throughflow the fluid rotation ratio k is no longer constant and varies with the radial position. Typically k increases radially inwards for centripetal throughflows. Möhring [6] formulates a differential equation for rotor-stator cavities with superposed throughflow. It accounts for wall friction at the stator and the rotor wall and also for the angular momentum of the throughflow which enters the cavity through a annular gap at the outer radius. Furthermore the angular momentum of the secondary flow in radial direction are considered. Wall shear stress is assumed to be of Blasius-type and the velocity distribution in the boundary layers to be according to the one-seventh power law. Correlations for the thicknesses of the boundary layers are taken from the case of a disk rotating in an idle environment and so the fluid rotational ratio is given by:

$$\frac{dk}{dx} = 0.07875 \frac{\pi\, \omega\, x^{8/5}}{Q\, Re_u^{1/5}} r_2^3 \left[\left(\frac{1 - k_0}{k_0} k \right)^{7/4} - (1 - k)^{7/4} \right] - 2\frac{k}{x} \tag{6}$$

where $x = \frac{r}{r_2}$ is the non-dimensional radius, Q the volumetric leakage flow and $Re_u = \omega\, r_2^2/\nu$ the rotational Reynolds number.

2.3.2 The Flow in an Annular Gap

An annular gap in the context of axial thrust balancing is formed by a stationary outer ring element and an inner rotating cylinder. The gap width s_{angap} is significantly smaller than the average radius r_{angap}. If there is an axial throughflow, which is characterized by $Re_{ax} = \frac{2\, s_{angap}\, \bar{c}_{ax}}{\nu}$ with the axial flow velocity $\bar{c}_{ax}$, a pressure loss Δp_{angap} will occur. The axial flow through the gap is superposed by a rotational flow with its characterizing Reynolds number $Re_{r,angap} = \frac{2\, s_{ax}\, \omega\, r_{angap}}{\nu}$. The magnitude of the rotational flow is greatly dependent on the amount of rotation before the gap. On the one hand the pressure drop across the gap consists of the lossy constriction of the flow at the gap entry, of the losses related to the formation of the developed gap flow and of the losses of the deceleration and the turbulent dissipation at the end of the gap. All the losses are summed up in the loss coefficientζ_{EA}: $\Delta p_{EA} = \frac{\rho}{2}\zeta_{EA}\bar{c}_{ax}^2$. On the other hand the pressure drop across the gap comprises the friction loss of the fully-developed gap flow: $\Delta p_\lambda = \lambda_{angap}\frac{\rho}{2}\frac{l}{2 s_{angap}\bar{c}_{ax}^2}$. Like presented in [12], the total pressure loss across the annular gap is given by

$$\Delta p_{angap} = \left(\zeta_{EA} + \lambda_{angap} \frac{l}{2\, s_{angap}} \right) \frac{\rho}{2} \bar{c}_{ax}^2 \tag{7}$$

and the volumetric gap throughflow by

$$Q_{angap} = 2\,\pi\, r_{angap}\, s_{angap} \sqrt{\frac{2}{\rho} \frac{\Delta p}{\zeta_{EA} + \frac{\lambda_{angap}\, l_{angap}}{2 s_{angap}}}}. \tag{8}$$

The friction coefficient λ_{angap} depends on the type of flow in the gap. For low Reynolds numbers Re_{angap} and $Re_{r,angap}$ the flow is laminar and friction is independent of the rotational speed. Annular gap flows in turbopumps for LRE are of turbulent character and according to Gülich [4] λ_{angap} can be calculated with

$$\frac{\lambda_{angap}}{\lambda_{0,angap}} = \left[1 + 0.19 \left(\frac{Re_{u,angap}}{Re_{angap}} \right)^2 \right]^{0.375} \tag{9}$$

DOI: 10.13009/EUCASS2017-40

with

$$\lambda_{0,angap} = \frac{0.31}{\left[log_{10}\left(0.135\frac{\varepsilon}{s_{angap}} + \frac{6.5}{Re_{angap}}\right)\right]^2} \tag{10}$$

being the friction coefficient for a non-rotating cylinder and ε the throatiness of the gap walls. The development of the fluid rotational ratio in axial direction in an annular gap can be quantified with

$$k = 0.5 + (k_{in} - 0.5)\, exp^{-\frac{\lambda_{angap}\, z}{4\, s_{angap}}\left(1+\frac{0.75}{1+4\left(\frac{Re_{angap}}{Re_{r,angap}}\right)^2}\right)}. \tag{11}$$

2.3.3 The Flow in an Axial Gap

An axial gap consists of two ring face elements which are at close distance and a flow perpendicular to the rotation axis runs between them. The gap width is significantly smaller than the inner radius of the faces and one of them rotates while the other face is at rest. Pressure losses in an axial gap are similar to those in an annular gap. At the entry of the gap there are losses because of the acceleration and constriction of the flow: $\Delta p_E = \frac{\rho}{2}\,\zeta_E\,\bar{c}_i^2$. Along the walls of the gap friction further increases the losses: $\Delta p_\lambda = \frac{\rho}{2}\frac{\lambda_{angap}\, r_i}{2\, s_{angap}}\bar{c}_i^2(1 - r_i/r_a)$. Furthermore there are additional losses at the end of the gap because of deceleration and turbulent dissipation: $\Delta p_A = \frac{\rho}{2}\zeta_A\,(r_i/r_a)^2\bar{c}_i^2$. The rotation of the fluid in the gap and therfore the centrifugal forces, which result in an increase in pressure in outward direction, are taken into account by $\Delta p_Z = \frac{\rho}{2}\,k^2\,\omega^2(r_a^2 - r_i^2)$. Also there is a nozzle effect which increases pressure for a throughflow inwards. Wagner [11] found for the volumetric throughflow of an axial gap

$$Q_{axgap} = 2\,\pi\, r_i\, s_{axgap}\sqrt{\frac{\rho}{2}\frac{\Delta p_{axgap} - k^2\,\omega^2\, r_a^2\,(1 - a_r^2)}{\zeta_E\, a_r^2 + \lambda_{axgap}\frac{r_i}{2\, s_{axgap}}(1 - a_r) + \zeta_A}}. \tag{12}$$

with $a_r = r_i/r_a$. The pressure distribution in the gap is given by

$$p_{axgap}(r) = p_E + \frac{\rho}{2}\,\bar{c}_i^2\left[\zeta_A + \frac{\lambda_{axgap}\, r_i^2}{2\, s_{axgap}}\left(\frac{1}{r_i} - \frac{1}{r}\right) - \frac{r_i^2}{r^2} + \frac{k_{axgap}^2\,\omega^2}{\bar{c}_i^2}(r_a^2 - r_i^2)\right] \tag{13}$$

and the axial force by

$$F_{axgap} = \int_{r_i}^{r_o} p_{axgap}(r)\, r\, dr. \tag{14}$$

λ_{axgap} is calculated with equations 9 and 10 and the Reynolds numbers $Re_{axgap} = \frac{2\, s_{axgap}\,\bar{c}_i}{\nu}\sqrt{a_r}$ and $Re_{r,axgap} = \frac{2\, s_{axgap}\,\omega\, r_a}{\nu}\sqrt{a_r}$.

3. Description of the Applied Methods

3.1 Analytical Method

The analytical calculation programs presented in this paper can determine the pressure distribution and the axial thrust acting on the backside of the impeller. Furthermore the volumetric leakage flow through the backside cavity is calculated. Input parameters include geometrical impeller, cavity and gap data, rotational impeller speed, suction pressure, impeller pressure head and rotational speed of the fluid at the impeller exit. The programs are subdivided into separate program modules for each particular flow affecting part of a balancing system, such as e.g. an axial gap or a rotor-stator cavity. All elements of a balancing system that affect the flow influence each other. Therefore the analytical formulations of all parts need to be solved in a combined context. Thus, the program blocks are linked by means of leakage flow and pressure loss. Because of continuity, the volumetric flow through each element has to be the same:

$$Q = Q_{rscav} = Q_{angap} = Q_{axgap}.$$

Also the sum of the pressure losses or respectively the pressure decreases of all elements must be equal to the impeller pressure head:

$$\sum_i \Delta p_i = \Delta p_{Imp} = p_2 - p_S\,. \tag{15}$$

The analytical equations of the balancing systems are solved iteratively. In the first iteration step generical initial values for the iterative variables are specified. The calculations done with these values result in new values for the iterative variables and with them the calculation process starts over. To avoid strong numerical oscillation of the solution values and therefore instabilities a damping coefficient d for the leakage mass flow variable is used. The iterative process stops as soon as the change in volumetric leakage flow Q is below a specified limit.

DOI: 10.13009/EUCASS2017-40

3.1.1 Program for a Balancing System with One Governing Gap

The calculation program for a balancing system with one governing gap consists of four program modules: an annular gap block, two rotor-stator cavity blocks and an axial gap block. Figure 2 shows the iterative calculation process for such a system. An iteration run starts with the calculation of the pressure loss Δp_{angap} across the annular gap and the fluid rotation ratio k_E at the end of the gap from the leakage flow Q^n and the fluid rotation ratio at the entry of the gap k_{in}. For that equations 7, 9, 10 and 11 are used. With k_E, Q^n and with equations 3, 4, 5 and 6 the rotor-stator cavity module for the section between the annular gap and the axial gap calculates the pressure decrease in the outer cavity Δp_{r-s}, the distribution of the fluid rotation ratio in the whole backside cavity $k(r)$ and the axial force F_{r-s} acting on the impeller in this section. With the pressure drops of both previous modules, $k(r)$, the suction pressure p_S and the impeller exit pressure $p_2 = p_S + \Delta p_{Imp}$, the pressure drop in the inner rotor-stator cavity Δp_B^n and the wall friction coefficient λ_{axgap}^n the program block for an axial gap determines the axial force F_{axgap} acting on the impeller in the gap, the new leakage flow Q^{n+1} and the new wall friction coefficient λ_{axgap}^{n+1}. The calculations in this module are based on equations 9, 10, 12, 14 and 15. The (last) program module for the rotor-stator cavity between the axial gap and the balancing holes determines the new pressure drop Δp_B^{n+1} and the axial force F_B of this section of the impeller backside cavity with $k(r)$ and equations 3 and 4. The pressure in the sector between the balancing holes and the hub is assumed to be equal to suction pressure. The axial force is given by: $F_s = p_S \pi \left(r_i^2 - r_H^2\right)$. The axial forces of each section are summed up to the total axial thrust on the backside of the impeller: $F_{bs} = F_s + F_b + F_{axgap} + F_{r-s}$.

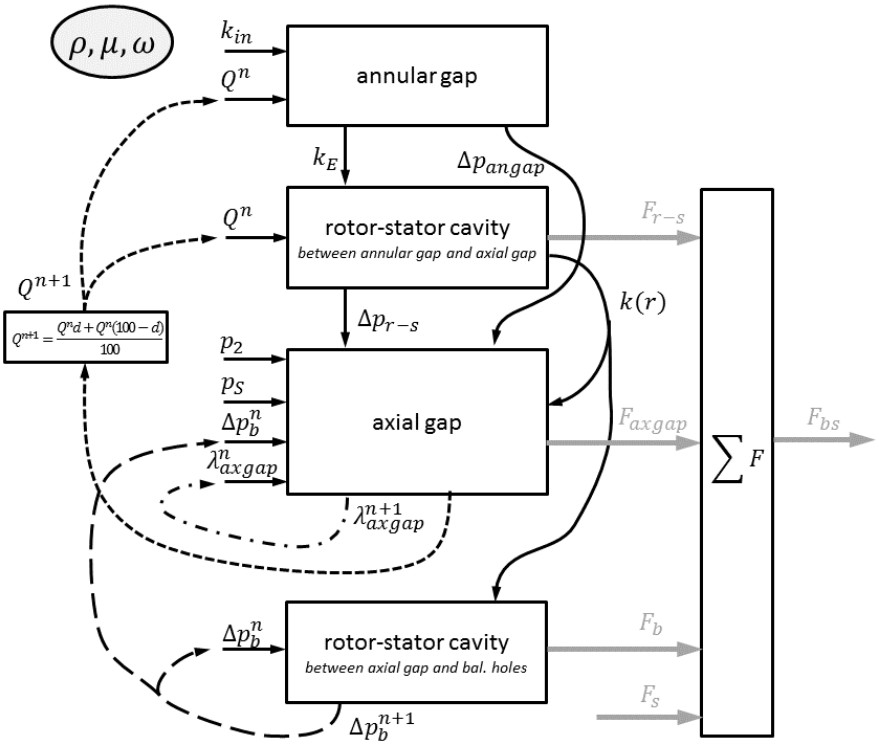

Figure 2: The iterative calculation process for the backside cavity of a balancing system with one governing gap

3.1.2 Program for a Balancing System with Two Governing Gaps

The calculations program for a balancing system with two governing gaps is similar to the program for a system with one governing gap. It also has two rotor-stator program modules and a block for an inner axial gap but for the annular gap module a second axial gap program block comes in place. Figure 3 shows the iterative calculation process for this kind of balancing system. An iteration run begins with the calculation of the pressure loss across the outer axial gap $\Delta p_{axgap,o}$ and the axial force in the gap $F_{axgap,o}$ which acts towards the hub side. From there on the calculation process is identical to the program for a balancing system with one governing gap. For a balancing system with two governing gaps the total axial thrust on the backside of the impeller is: $F_{bs} = F_s + F_b + F_{axgap,i} + F_{r-s} - F_{axgap,o}$.

DOI: 10.13009/EUCASS2017-40

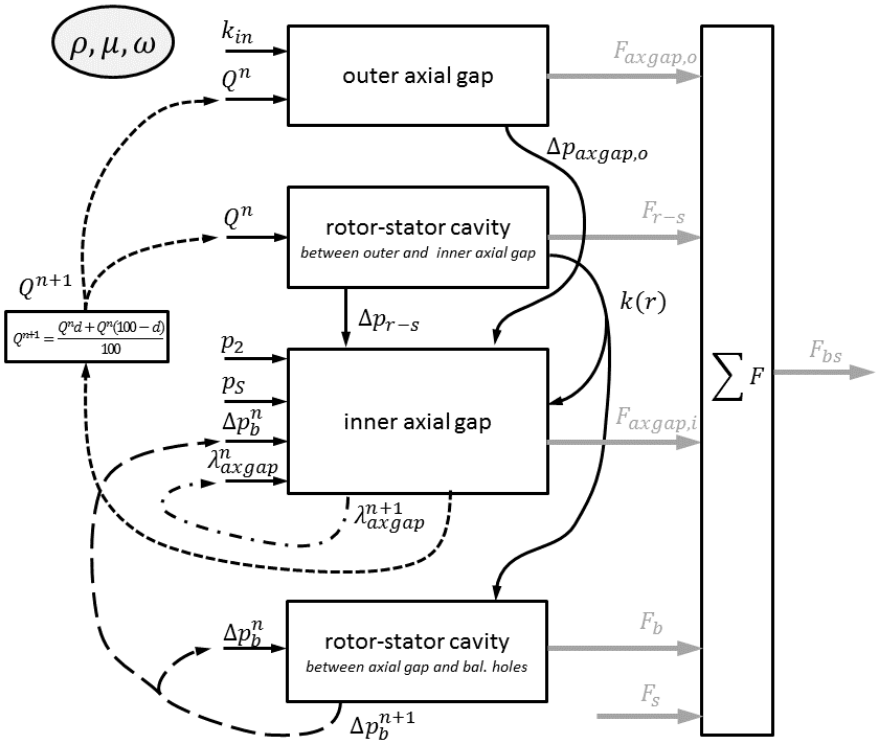

Figure 3: The iterative calculation process for the backside cavity of a balancing system with two governing gaps

3.2 Numerical Method

To assess the functionality and the calculated values of the programs presented, numerical RANS flow simulations are carried out. In a first step, the flow in a rotor-stator cavity with superposed through-flow is analyzed. In the next step, the CFD model of the rotor-stator cavity is adapted to the geometry of the investigated impeller, and extended to represent the backside cavity of the impeller of either a balancing system with one governing gap or a system with two governing gaps. The extended models also include the particular gap configuration of the balancing system and a further gap for the through- flow to return to both the main and impeller exit streams. The numerical procedure for all cases is based on the Finite-Volume Method using collocated, structured grids, and the axisymmetry hypothesis in the mean section. The solving process is done with the commercial software ANSYS CFX 16.2 [1] with convergence criteria set to 10^{-5} RMS.

3.2.1 Simulation Model of a Rotor-Stator Cavity

The experiments from Poncet with water in the gap between a rotating disk at high speeds and a non-rotating casing wall are compared to the numerical predictions. The geometry of the CFD model for a rotor-stator cavity is based on the experimental setup in that publication [7]. The simulation domain is a 1° segment of the entire cavity with an inflow opening at the top for the through-flow to enter, and an exit opening at the hub. The grid consists of 279 cells in the radial direction and 79 cells in the axial direction. This grid has proven to be sufficient to provide grid-independent solutions. The grid has been refined at the rotor and the stator walls to resolve the boundary layers. The fluid is water at 25 °C (density $\rho_W = 997\,\frac{kg}{m^3}$, dynamical viscosity $\mu_W = 8.899 \cdot 10^{-4}\,\frac{kg}{m\,s}$) assumed to be incompressible and isothermal. Turbulence is modeled with Menter's *SST-k-ω* model, which has already successfully been applied to this kind of flow [2]. At the static walls, the velocity is set to zero, and the tangential velocity of the rotor wall is $\omega\, r$. The distribution of the tangential velocity at the entry gap is linear, from $c_\Theta = \omega R_2$ at the outer edge of the disk to $c_\Theta = 0$ at the outer stator wall. In the axial direction, a parabolic velocity profile is set according to the through-flow rate C_W with $c_z = C_W\, \nu\, R_2 / \left[\pi \left(R_3^2 - R_2^2\right)\right]$ at the peak and $c_z = 0$ at the outer edge of the disk as wells as at the outer stator wall. There is no flow in radial direction at the entry opening. Latter boundary conditions are set as proposed by Poncet, Chauve and Schiestel. At the exit opening an outward mass flow with $\dot{m} = C_W\, \nu\, R_2\, \rho_W / 360$ is defined.

DOI: 10.13009/EUCASS2017-40

3.2.2 Simulation Models of Active Balancing Systems

The dimensions of the balancing systems are based on the geometry of an LOx impeller for a 120kN expander cycle engine under development in the project KonRAT [9]. Details on design and requirements for the turbopump can be found in [5] and [8]. In the preliminary KonRAT design the outer impeller diameter r_2 is 50 mm. Both simulation domains, for a balancing system with one governing gap and for a system with two governing gaps, are one 1° segment of the backside cavity of the impeller. They both include half of the main flow at the impeller exit where the leakage flow branches off, an inner axial gap with a width between 0.05 *mm* and 0.45 *mm* (depending on the case) and a back flow channel of 0.7 *mm* width. This represents balancing holes since they can not be modeled in one segment. All narrow gaps have chamfers of 0.1 $mm \times 45°$ at their entries and exits. The width of the backside cavity is set to 2.05 *mm* for which the relation $G = b_{r-s}/r_2 = 0.0036$ is the same as in [7]. The model of the system with one governing gap has an annular gap with a width of 0.25 *mm* and a length of 3 *mm*. The model of a system with two governing gaps has a further axial gap with a length of 5 *mm* and the backside cavity is extended to 58.2 *mm*. Details of the domains' dimensions can be seen in figures 7 and 9. The meshes are refined at all walls of the cavity, gaps, and resolve the boundary layers down to the viscous sublayer. The faces of the cells are aligned with the flow where possible, and cover roughly 220000 cells (system with one governing gap) or 286700 cells (system with two governing gaps) respectively. The fluid is defined as liquid oxygen at 90.2 *K* (density $\rho_{LOx} = 1130\ \frac{kg}{m^3}$, dynamical viscosity $\mu_{LOx} = 1.85 \times 10^{-4}\ \frac{kg}{m\,s}$) which is considered to be incompressible and isothermal. Turbulence is modeled with Menter's *SST-k-ω* model. At the impeller exit profiles according to the one-seventh power law for the tangential and meridional velocity c_Θ and c_r are set so that they are zero at the impeller wall and peak in the main channel mean with w_{2u} and w_{2m}. In the mean of the channel a symmetry plane is defined. Static pressure is specified at the entry to the volute ($p_{Vol} = p_s + \Delta p_{Imp}$) and at the back flow channel exit ($p_b = p_s$). At all rotor and stator walls all velocity components are set to zero, except for the tangential velocity c_Θ at the rotor which is $\omega\, r$.

4. Verification and Validation of the Applied Methods

4.1 Numerical Validation Case

With the CFD model of a rotor-stator cavity described earlier simulations were carried out at a Reynolds number of $Re = \omega\, r_2^2/\nu = 1 \times 10^6$ with three throughflow rates and at $Re = 4,15 \times 10^6$ with $C_W = 5929$. The computed profiles of the non-dimensional tangential and radial velocities $c^*_\Theta = c_\Theta/(\omega\, r)$ and $c^*_r = c_r/(\omega\, r)$ at the radial location $x = 0.56$ are presented in figure 4 and compared to LDA data from the experiments in literature [7] and the predictions of the Reynolds stress turbulence model therein. $z^* = z/b_{r-s}$ is the non-dimensional axial coordinate with $z^* = 0$ corresponding to the rotor side and $z^* = 1$ to the stator side. At low centripetal throughflow rates the fluid in the core region rotates slower than the rotor and begins to overtake latter at higher rates. With an increased Reynolds number of $Re = 4.15 \times 10^6$ the relative rotation speed of the core is lower than with $Re = 1 \times 10^6$. With increasing throughflow the radial velocity profile becomes more and more centripetal. Increased disk speed boosts the centrifugal forces at the rotor and therefore rises the outward flow at this side of the cavity. The results of the conducted simulations with the SST model are in very good agreement with the experimental data at all throughflow rates and Reynolds numbers. There is a minimal discrepancy to the Reynolds stress model of Poncet [7]. The velocity profiles for $Re = 1 \times 10^6$ and $C_W = 5929$ at other radial locations (not illustrated) also match the LDA data in a very satisfactory way and are slightly closer to the measured values than the Reynolds stress model presented in literature.

In figure 5 the pressure coefficient $C_p = P^*(x) - P^*(x = 0.92)$ with $P^* = 2\, p/(\rho_W\, \omega\, r_2^2)$ is plotted versus the non-dimensional radius x for $Re = 1 \times 10^6$ and three throughflow rates. The predictions of the SST model are compared to the Reynolds stress model of Poncet [7] and their experimental pressure data. For all throughflow rates pressure decreases towards the center of the cavity. With higher throughflow rates the pressure drop increases (lower absolute values). This is in accordance with theory (see equation 3) and measurements. The overall agreement between the predictions with the SST turbulence model and the pressure measurements is good. For all throughflow rates investigated there is some deviation. Predictions of the pressure profiles in the cavity with the Reynolds stress model in literature are more accurate than predictions with the SST model. Still the SST model implemented in ANSYS CFX 16.2 is a good compromise in terms of prediction quality, convergence and modeling effort.

DOI: 10.13009/EUCASS2017-40

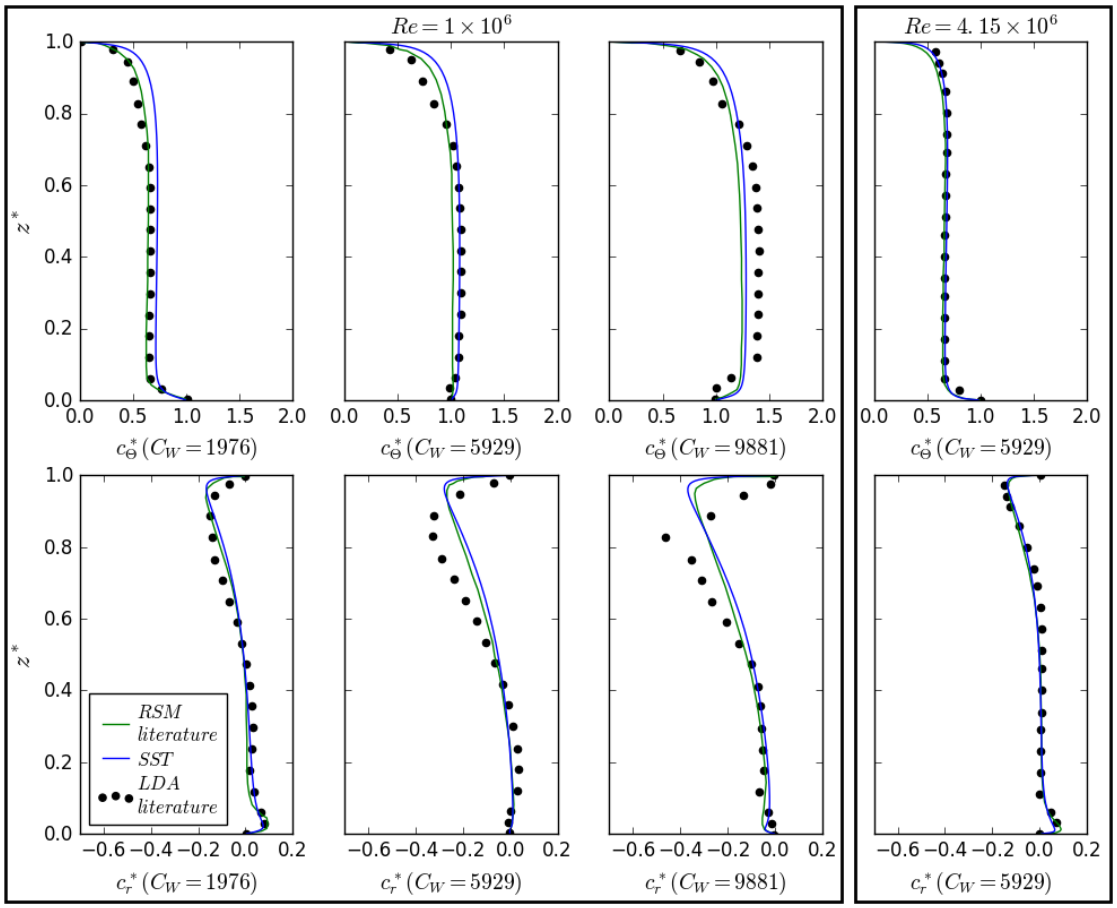

Figure 4: The computed profiles of the non-dimensional tangential and radial velocities $c^*_\Theta = c_\Theta/(\omega\, r)$ and $c^*_r = c_r/(\omega\, r)$ at the radial location $x = 0.56$ in comparison to LDA data from the experiments in literature [7] and the predictions of the Reynolds stress turbulence model therein for two Reynolds numbers and three throughflow rates

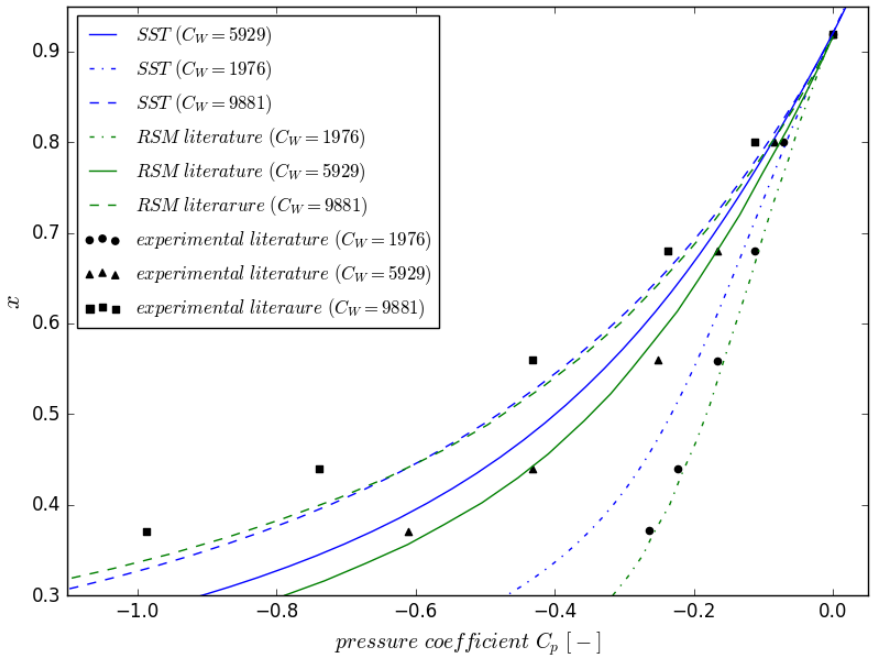

Figure 5: The pressure coefficient C_p from simulations with the SST model compared to experimental data and the Reynolds stress model from literaure [7] for three throughflow rates

DOI: 10.13009/EUCASS2017-40

4.2 Verification of the Analytical Model

Figure 6 presents the fluid rotational ratio k_{CFD} in the mean of the cavity taken from the simulation results at $Re = 1{\times}10^6$ with three throughflow rates and at $Re = 4.15 \times 10^6$ with $C_W = 5929$. Moreover the plot shows the fluid rotational ratio k_{calc} calculated with the program module for a rotor-stator cavity. For latter calculation the fluid rotation ratio at the throughflow entry opening is defined as $k_E = 0.5$ which represents the average value of the linear profile of the tangential velocity. All graphs show increasing values towards the center of the cavity. With rising throughflow rates the fluid rotation intensifies. This is in accordance with the conservation of angular momentum and the boosting influence of a centripetal throughflow on the fluid rotation in the cavity. There are small discrepancies in the region next to the hub. Apart from that agreement between both methods is very good for all cases investigated.

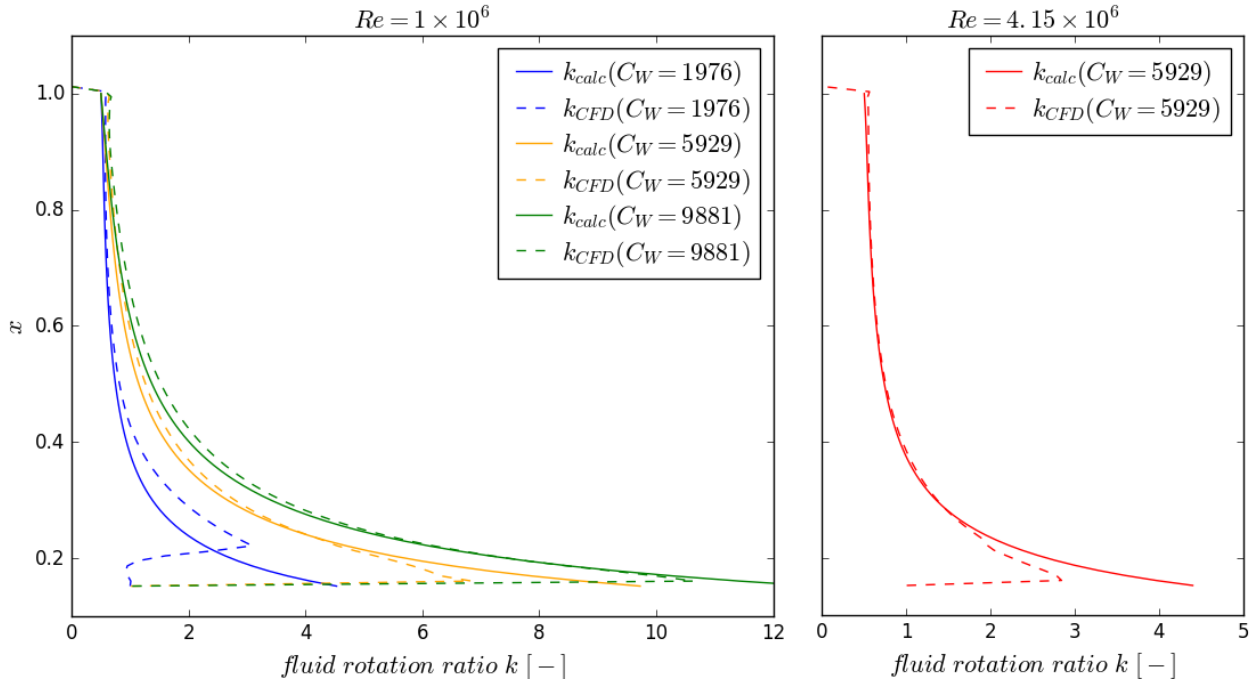

Figure 6: The fluid rotation ratio k_{calc} from analytical calculations compared to the ratio k_{CFD} taken from the simulation results for $Re = 1 \times 10^6$ (left) and $Re = 4.15 \times 10^6$ (right) and three throughflow rates

Table 1 shows the pressure drop Δp in the cavity from the outer edge of the disk ($x = 1.0$) to the hub ($x = 0.152$) along with the axial force F_R acting on the rotor for the investigated cases at $Re = 1 \times 10^6$ and $Re = 4.15 \times 10^6$ and for throughflow rates of $C_W = 1976$, 5929 and 9881. The pressure level at $x = 1.0$ is defined to be the reference pressure of $p_{ref} = 0\ bar$. The pressure drop in the cavity is calculated from the fluid rotation ratio k_{calc} which is determined using equation 6 and from the fluid rotation ratio k_{CFD} extracted from the flow simulation results. Also the pressure drop is identified from latter (Δp_{CFD}) as well as the axial force ($F_{R,CFD}$). Moreover the axial thrust is calculated from the fluid rotations ratio k_{calc} and k_{CFD}. The pressure drop increases with intensifying throughflow and with higher Reynolds numbers which corresponds to theory (see section 2.3.1 and equation 3). $\Delta p(k_{CFD})$ and Δp_{CFD} show excellent agreement for all cases. This proves that equation 3 is valid. All values of $\Delta p(k_{calc})$ and $F_R(k_{calc})$ match the pressure drop Δp_{CFD} and respectively the axial thrust $F_{R,CFD}$ taken from the simulation results in a very good way. Therefore there is a very satisfying agreement between predictions with the differential equation 6 and the CFD predictions. Conformity between $F_R(k_{CFD})$ and $F_{R,CFD}$ verifies the integration method used in the rotor stator program module to calculate the axial force from the fluid rotation ratio k.

DOI: 10.13009/EUCASS2017-40

Table 1: The pressure decrease in the rotor-stator cavity Δp and the resulting axial force F_R on the rotor identified in the simulations and those calculated from the fluid rotation ratio k_{calc} from equation 6 and from the fluid rotation ratio k_{CFD} taken from simulation results at two Reynolds numbers and three throughflow rates

Re	C_W	$\Delta p(k_{calc})$	$\Delta p(k_{CFD})$	Δp_{CFD}	$F_R(k_{calc})$	$F_R(k_{CFD})$	$F_{R,CFD}$
1×10^6	1976	−0.0638 *bar*	−0.0655 *bar*	−0.0634 *bar*	−267.4 *kN*	−320.0 *kN*	−318.6 *kN*
1×10^6	5929	−0.2045 *bar*	−0.1873 *bar*	−0.1800 *bar*	−458.0 *kN*	−542.7 *kN*	−531.7 *kN*
1×10^6	9881	−0.3266 *bar*	−0.3269 *bar*	−0.2987 *bar*	−594.4 *kN*	−718.7 *kN*	−693.9 *kN*
4.15×10^6	5929	−1.0578 *bar*	−0.9301 *bar*	−0.9343 *bar*	−4536.7 *kN*	−4793.7 *kN*	−4828.7 *kN*

5. Results

The results of the analytical calculation programs and of the RANS CFD simulations are presented for the geometry and operating conditions of the impeller under development in the project KonRAT. Suction pressure p_S is 9 *bar*, impeller pressure head Δp_{Imp} is 45 *bar* (independent from the impeller rotation speed ω), tangential velocity at the impeller exit c_Θ is 26.58 $\frac{m}{s}$ (varies linearly with ω) and the meridional velocity at the impeller exit is 10.38 $\frac{m}{s}$ (independent from ω). The geometry of the impeller and of all narrow gaps are presented in section 3.2.2. The loss coefficient ζ_E for the entry of an axial gap is set to 0.15 and the coefficient ζ_A for the exit to 1.0. The assessment of the analytical and the numerical methods is carried out at three rotational speeds: *10000 rpm*, *15000 rpm* and *20000 rpm*.

5.1 Balancing System with One Governing Gap

For the analytical calculation of a balancing system with one governing gap the fluid rotation ratio k_{in} at the entry of the annular gap is determined from the tangential velocity at the impeller exit c_Θ. Furthermore the coefficient for losses at the entry and at the exit of the annular gap ζ_{EA} is set to 1.1. Figure 7 illustrates the pressure profile in the backside cavity of the impeller $p(x)$ along with the distribution of the fluid rotation ratio $k(x)$ from the analytical calculation and the RANS simulation at *10000 rpm* and for an axial gap width s_{axgap} of 0.15 *mm*. Furthermore the figure shows the dimensions of the backside of the impeller and of the gaps. This is an example of the output of both calculations methods. Most of the other investigated cases show similar behavior. The fluid rotation ratio k is about 0.7 at $x = 1.0$ and increases towards the center for both methods. Inwards from the axial gap k_{CFD} starts to decrease while k_{calc} continues to rise. The calculated values of the fluid rotation ratio k excellently match between the annular gap and the inner radius of the axial gap. In the inner part of the cavity a complex flow can be observed which the analytical method doesn't account for and so k_{calc} deviates from k_{CFD}. For both methods there is a pressure loss across the annular gap at the outer radius of the impeller. Then pressure continues to decrease in the cavity between the annular and the axial gap. At the entry to the axial gap there is another pressure loss and pressure keeps on decreasing in the gap. Between the exit of the axial gap and the back flow channel pressure decreases further. In the section between back flow channel and the hub the pressure is approximately constant. The calculation results of the pressure are in very good agreement with pressure values determined with the analytical method. These are overall slightly higher. Consequently the values of the calculated axial forces and of the volumetric leakage flow show a very good match: 27.29 *kN* and 1.227 l/s from analytical calculation compared to 25.74 *kN* and 1.268 l/s from numerical prediction.

In figure 8 all results for the axial force F_{bs} and the volumetric leakage flow Q_{bs} of the analytical and numerical method are plotted versus an axial gap width s_{axgap} up to 0.5 *mm* at three rotation speeds. Analytical calculations show decreasing axial force with increasing gap width for all rotation speeds. At *10000 rpm* a almost linear behavior with an overall stiffness of about 7.5 kN/mm can be observed. At higher rotation speeds stiffness decreases and only for a gap width smaller than 0.15 *mm* there is a notable change in axial force. The numerical predictions generally have a negative offset for all cases and gap widths which is because of the pressure profiles being at a slightly lower level than the analytically calculated ones. Overall they reflect the behavior of the analytical calculations but show a little increasing tendency from $s_{axgap} = 0.15$ *mm* towards greater gap widths for higher rotation speeds. The analytically calculated values for the volumetric leakage flow Q_{bs} show an increase with bigger gap widths and a decrease with rising rotational speeds. The numerical results excellently match the analytical values for *10000 rpm*. At higher rotation speeds of *15000 rpm* and *20000 rpm* there is some discrepancy but still both methods indicate the same behavior of the leakage. Overall there is very good agreement for the axial force and good agreement for the leakage.

DOI: 10.13009/EUCASS2017-40

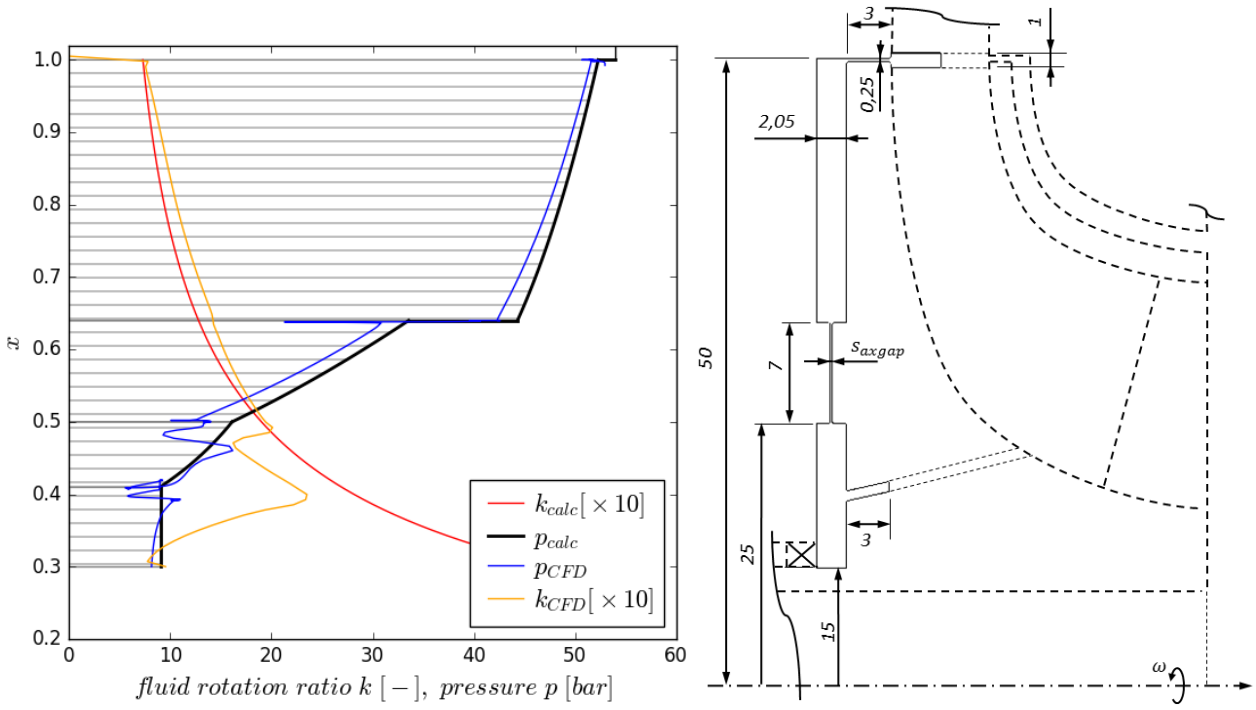

Figure 7: The pressure profile $p(x)$ and the distribution of the fluid rotation ratio $k(x)$ in the backside cavity of the impeller from the analytical and the numerical method (left) along with the dimensions of the simulation domain in millimeters (right) for a balancing system with one governing gap

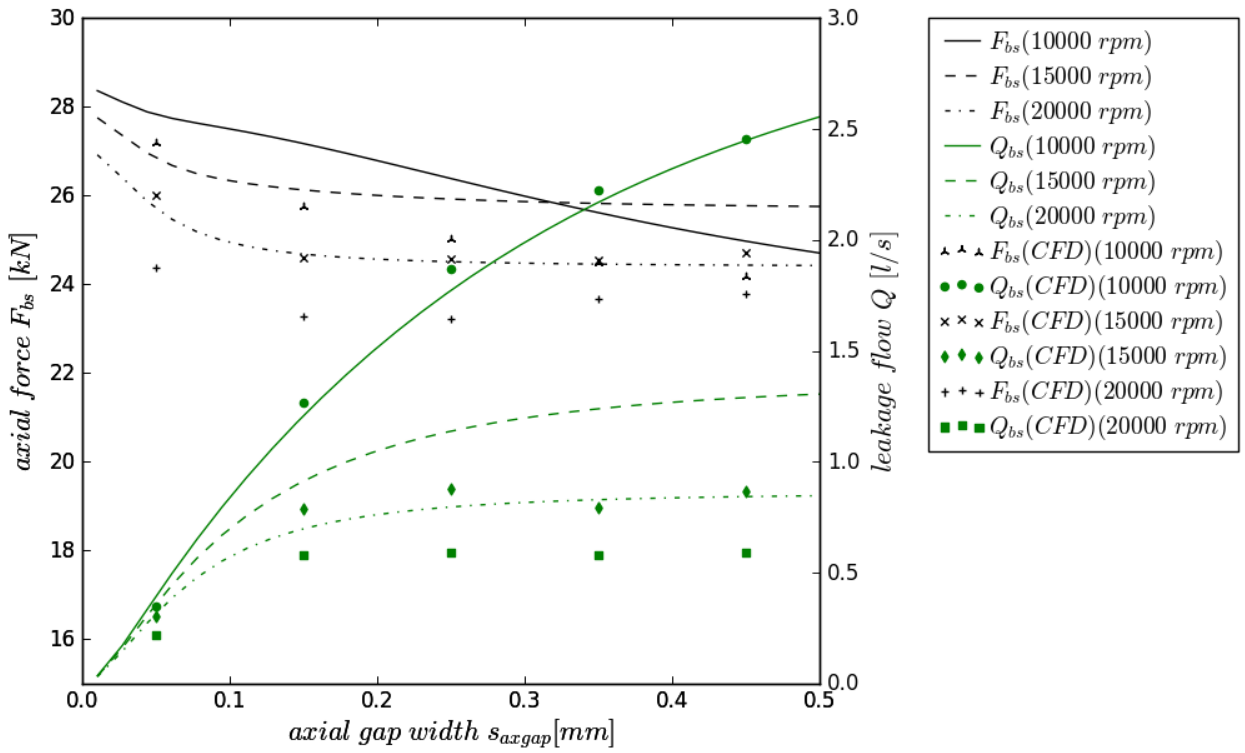

Figure 8: The results of the analytical and the numerical method for the axial force F_{bs} and the leakage Q_{bs} of a balancing system with one governing gap plotted versus the axial gap width s_{axgap} for three rotations speeds

DOI: 10.13009/EUCASS2017-40

5.2 Balancing System with Two Governing Gaps

The fluid rotation ratio $k(x)$ and the pressure profile $p(x)$ in the backside cavity of the impeller from analytical calculation and from numerical simulation are presented in figure 9 for an axial balancing system with two governing gaps. It is an exemplary case at *10000 rpm* with equal axial gap widths ($s_{axgap,i} = s_{axgap,o} = 0.25\ mm$). The fluid rotation ratio k starts at around 0.6 at the outer radius of the backside cavity and increases towards the center for both methods. At the back flow channel k_{CFD} drops while k_{calc} continues to rise. The distributions of k show an excellent match. The deviation in the region next to the hub is because the analytical method does not consider the complex flow there. Both methods show a very similar pressure distribution. Starting from the impeller exit pressure there is a pressure drop at the entry to the outer axial gap. In the gap pressure increases because of the dominating centrifugal forces. From the outer radius of the backside cavity pressure decreases towards the center. In the inner part of the cavity the behavior of pressure is identical to the system with one governing gap. The part of the outer axial gap in the pressure profile is marked with grey color because there the pressure acts contrary to the suction side. The pressure profiles of both methods are in very good agreement. The pressure values of the analytical calculation are somewhat higher than the numerical prediction between the axial gap exit and the back flow channel. The calculated values of the axial force F_{bs} and the volumetric leakage flow Q_{bs} reflect that observation: 26.43 kN and 1.935 l/s from analytical calculation in comparison to 25.70 kN and 1.989 l/s from numerical simulation.

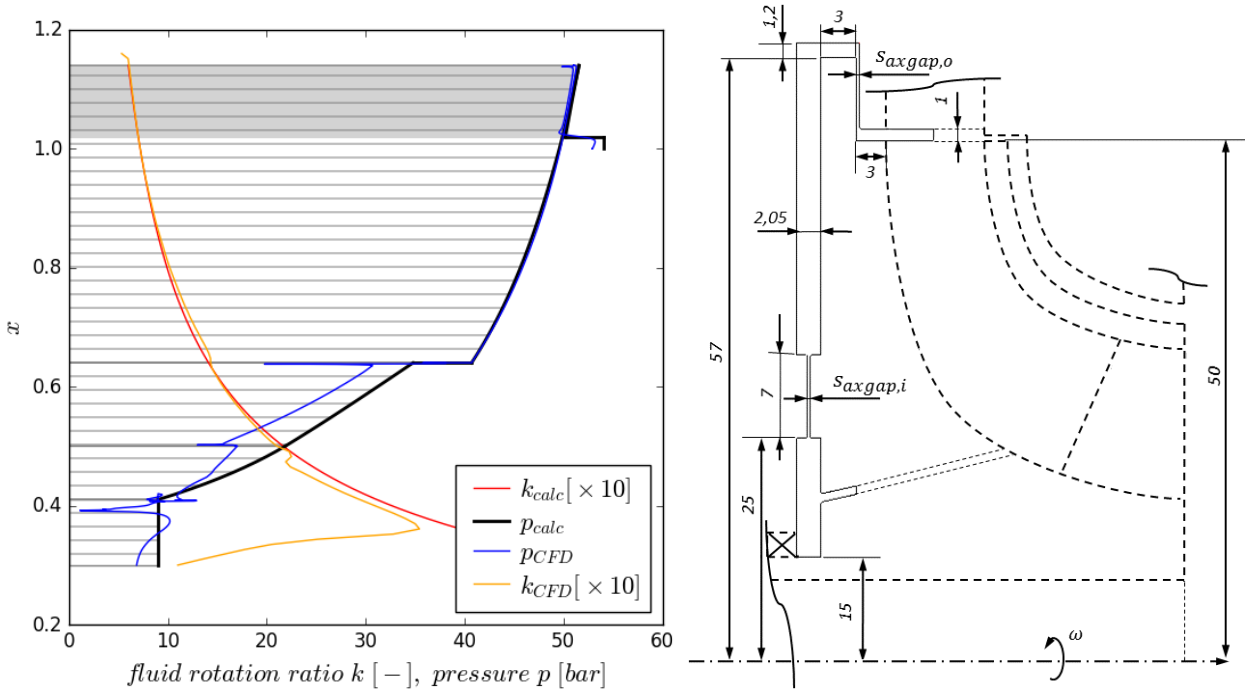

Figure 9: The pressure profile $p(x)$ and the distribution of the fluid rotation ratio $k(x)$ in the backside cavity of the impeller from the analytical and the numerical method (left) along with the dimensions of the simulations domain in millimeters (right) for a balancing system with two governing gaps

Figure 10 illustrates all results for the axial force F_{bs} and volumetric leakage flow Q_{bs} from analytical calculations and numerical computations for a rotor displacement Δs at three rotation speeds. For $\Delta s = 0.0\ mm$ the inner axial gap width is 0.35 *mm* and the outer axial gap width is 0.15 *mm*. Both methods show a decreasing axial force when the rotor moves towards the suction side. After a first steep part the gradients of the analytical graphs decrease. Towards higher rotor displacements stiffness increases again and for $\Delta s > 0.0\ mm$ the force characteristic gets very steep. For higher rotation speeds this behavior becomes more prominent. The numerical results are in excellent agreement with those analytically calculated and reflect the behavior mentioned before. The volumetric leakage flow calculated with the analytical method is zero at the ends of the displacement range ($\Delta s = -0.35\ mm$ and $\Delta s = 0.15\ mm$) and peaks at around $\Delta s = -0.05\ mm$ for all rotation speeds. The leakage flow gets less with rising impeller speed. Numerical simulations confirm those observations and both methods are in excellent agreement.

DOI: 10.13009/EUCASS2017-40

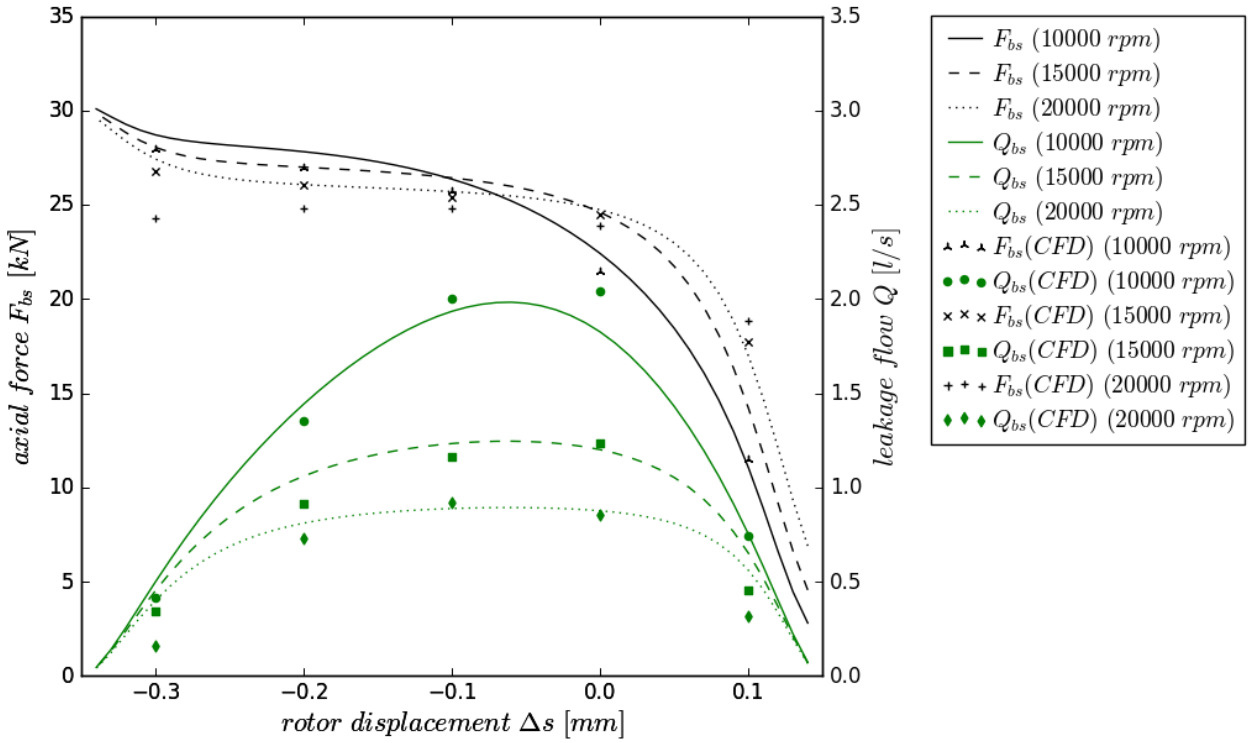

Figure 10: The results of the analytical and the numerical method for the axial force F_{bs} and the leakage Q_{bs} of a balancing system with two governing gaps plotted versus the rotor displacement Δs for three rotation speeds

6. Conclusion

For the simple case of a rotor-stator cavity only, the applied numerical method shows very good agreement in comparison to experimental data taken from literature. The results are even comparable to existing CFD results with a Reynolds stress tensor turbulence model. The CFD results of the rotor-stator cavity are also used to verify and validate the analytical model for the *k* ratio distribution. Once a again, good agreement could be found. Therefore both methods are validated and they can be used for the presented case study. Two types of active balancing systems are modeled, a system with one governing gap and a system with two governing gaps. The geometry and the boundary conditions are representative for a 120 *kN* rocket engine LOx turbopump impeller. The gap flow program well predicts both, the *k* ratio distribution and the pressure profile. Even for three different rotation speeds and over a wide range of axial displacement the analytical solutions provide satisfying results for the axial forces and the leakage mass flow compared to the simulations. For the one gap system a discrepancy to the simulation results can be found. In future, the presented programs will be joined into the existing analytical prediction tool for the entire turbopump [10]. A loss coupling to a rotordynamic tool is also planned. The rotor displacement would be an input from the rotor analysis and calculated axial force will be returned to the dynamic tool. The analytical programs are rapid, reliable, and simple tools, which are helpful in the iterative design and assessment of active axial balancing systems.

7. Acknowledgments

The KonRAT project is supported by Ludwig Bölkow Campus, funded by the Bavarian government under grant number: LABAY83E. The good cooperation between the project partners is kindly acknowledged.

DOI: 10.13009/EUCASS2017-40

References

[1] ANSYS, Inc.: ANSYS CFX Turbomachinery Simulation, `http://www.ansys.com/Products/Fluids/ANSYS-CFX`.

[2] Beck, P., Wagner, B., Haidn, O.: The influence of secondary flows in the thrust acting on the axis of a radial LOx pump. In: *12th European Conference on Turbomachinery Fluid Dynamics and Thermodynamics*. 2017.

[3] Daily, J. W., Nece, R. E.: Chamber dimension effects on induced flow and frictional resistance of enclosed rotating disks. *Journal of Basic Engineering*. 82(1):217-230. 1960.

[4] Gülich, J. F.: *Centrifugal pumps*. Springer Verlag. 2013.

[5] Maeding, C., Souverein, L., Hummel, D., Koenigbauer, S., Wagner, A., Alting, J.: A preliminary design study for an expander LOX turbopump. In: *6th European Conference for Aeronautics and Space Sciences*, 2015.

[6] Möhring, U. K.: *Untersuchung des radialen Druckverlaufes und des übertragenen Drehmomentes im Radseitenraum von Kreiselpumpen bei glatter, ebener Radseitenwand und bei Anwendung von Rückenschaufeln.* PhD Thesis. Braunschweig, Technische Universität Carolo-Wilhelmina zu Braunschweig. 1976.

[7] Poncet, S., Chauve M.-P., Schiestel, R.: Batchelor versus Stewartson flow structures in a rotor-stator cavity with throughflow. *Physics of Fluids*. 17(7):075110-15. 2005.

[8] Souverein, L., Maeding, C., Aichner, T., Ivancic, B., Wagner, A., Frey, M.: Design and tool anchoring for a 120kN expander cycle rocket engine LOx turbopump. In: *6th European Conference for Aeronautics and Space Sciences*, 2015.

[9] Veggi, L., Pauw, J. D., Wagner, B., Godwin, T., Haidn, O.: Numerical and experimental activities on liquid oxygen turbopumps. In *5th Conference on Space Propulsion*, 2016.

[10] Wagner, B., Stampfl, A., Beck, P., Veggi, L., Pauw, J. D., Kitsche, W.: Untersuchungen zu Sekundärsystemen in Turbopumpen für Flüssigkeitsraketenantriebe. In: *65. Deutscher Luft- und Raumfahrtkongress*, 2016.

[11] Wagner, W.: *Experimentelle Untersuchungen an radial durchströmten Spaltdichtungen*. Braunschweig. PhD Thesis. Technische Universität Carolo-Wilhelmina zu Braunschweig. 1972.

[12] Weber, D.: *Experimentelle Untersuchungen an axial durchströmten kreisringförmigen Spaltdichtungen für Kreiselpumpen*. PhD Thesis. Technische Universität Carolo-Wilhelmina zu Braunschweig. 1971.

[13] Zilling, H.: *Untersuchung des Axialschubs und der Strömungsvorgänge in den Radseitenräumen der einstufigen radialen Kreiselpumpe mit Leitrad*. PhD Thesis. Universität (TH) Karlsruhe. 1973.